ACS APPLIED MATERIALS & INTERFACES

Research Article

Cite This: ACS Appl. Mater. Interfaces 2019, 11, 957−962

www.acsami.org

Revealing the Degradation Mechanism of $LiMn_xFe_{1-x}PO_4$ by the Single-Particle Electrochemistry Method

Weiyuan Huang,[†] Jiangtao Hu,[†] Luyi Yang,* Wenguang Zhao, Ziqi Wang, Hongbin Wang, Zheng Guo, Yiwei Li, Jiajie Liu, Kai Yang, and Feng Pan*

School of Advanced Materials, Peking University Shenzhen Graduate School, Shenzhen 518055, China

Supporting Information

ABSTRACT: The commercial application of $LiMn_xFe_{1-x}PO_4$ materials has always been a great challenge because of their unsatisfactory structure stability during cycling and the safety issue. Herein, single-particle (SP) electrodes, where aggregated $LiMn_xFe_{1-x}PO_4$ is dispersed into SPs so they can distribute homogeneously in the carbon-nanotube networks, have been prepared and characterized to probe the degradation mechanism of $LiMn_xFe_{1-x}PO_4$ for the first time. Compared with a conventionally prepared cathode, the SP $LiMn_xFe_{1-x}PO_4$ cathode shows prominent capacity-fading with cycle numbers, which can be attributed to the formation of the MnF_2 nanocrystals on the surface of $LiMn_xFe_{1-x}PO_4$ because of the reaction between F^- and dissolved Mn^{2+} at the interface between the electrolyte and $LiMn_xFe_{1-x}PO_4$. The different electrochemical behaviors can be ascribed to $LiMn_xFe_{1-x}PO_4$ SPs surface reconstruction with MnF_2 nucleation and growth by the interfacial reactions. In addition, by applying a thin protecting layer of Al_2O_3 on the surface of $LiMn_xFe_{1-x}PO_4$, the interfacial side reactions can be suppressed. This work demonstrates that the SP method is a powerful tool to extract the information of interfacial reactions, which sometimes appear to be negligible compared with bulk reactions.

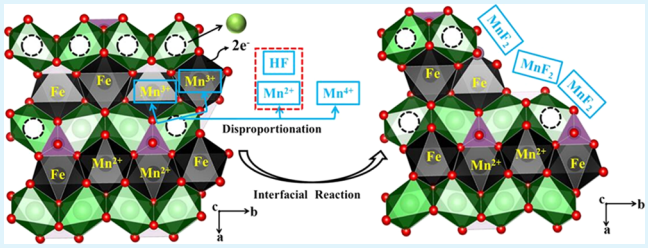

KEYWORDS: *single-particle, lithium iron manganese phosphate, lithium-ion battery, capacity-fading, surface degradation*

INTRODUCTION

Olivine $LiFePO_4$ is one of the most widely used cathode materials for lithium-ion batteries (LIBs) because of its low cost, safety, and great cyclic stability.[1−3] However, as it is restricted by its relatively low redox potential (3.4 V vs Li/Li^+), many researches turn to focus on other olivine-type cathode materials. For instance, $LiMnPO_4$, which has a much higher working potential (4.1 V vs Li/Li^+) owing to the Mn^{2+}/Mn^{3+} redox pair, is considered as a promising cathode material for the current commercial LIB system.[4] This ideal redox voltage can meet the demand of high energy density without decomposing the carbonate ester-based electrolyte.[5−7] However, the intrinsic drawbacks of $LiMnPO_4$, such as poor electrical conductivity ($\sim 10^{-10}$ S cm^{-1}) and low ionic diffusion coefficient ($\sim 10^{-16}$ cm^2 S^{-1}), have prevented it from delivering its theoretical capacity of 170 mA h g^{-1}.[5,8] One feasible approach is to partially substitute Fe with Mn to improve the operating potential of $LiFePO_4$. Padhi et al. first reported their systematic studies of $LiMn_xFe_{1-x}PO_4$ during charge and discharge and concluded that the presence of Fe could stabilize the Mn^{2+} because of the superexchange interaction between Fe^{3+}−O−Mn^{2+}.[3]

Nevertheless, after the introduction of Mn^{2+}, $LiMn_xFe_{1-x}PO_4$ still suffers from poor electronic conductivity, Jahn−Teller distortion of Mn^{3+} ions, and larger volume change during charge−discharge processes.[9−13] In addition, as the interface between the electrode and electrolyte interface is an active site for electronic and ionic transfer, the interfacial reconstruction is also crucial for the electrochemical performances of active materials.[14,15] Therefore, understanding the degradation mechanism by probing surface reconstruction and new specie growth on a cathode material is essential to designing active materials with good chemical/electrochemical stability. Previously, by developing ultrathin single-particle (SP) electrodes, where $LiFePO_4$ nanoparticles are uniformly distributed in the carbon nanotube network, the electrochemical behavior of single $LiFePO_4$ particles is investigated.[16] Herein, the SP electrochemical method is applied for the first time in order to study the intrinsic electrochemical behavior and surface reconstruction mechanism of SP $LiMn_{0.54}Fe_{0.46}PO_4$ (LMFP). Compared with a conventionally prepared cathode, the SP LMFP cathode exhibits a more prominent capacity-fading with cycle numbers. This deterioration can be attributed to the formation of the MnF_2 nanocrystals on the grain surface of LMFP, which results from the reaction between F^- and dissolved Mn^{2+} at the LMFP/electrolyte interface.

RESULTS AND DISCUSSION

The chemical composition of the cathode material is determined to be $LiMn_{0.54}Fe_{0.46}PO_4$ via inductively coupled

Received: October 29, 2018
Accepted: December 5, 2018
Published: December 5, 2018

DOI: 10.1021/acsami.8b18930
ACS Appl. Mater. Interfaces 2019, 11, 957−962

plasma (ICP) measurement (see Table S1). First, X-ray diffraction (XRD) measurement is carried out to study the crystal structure of the synthesized LMFP@C. As shown in Figure 1a, an olivine-type structure with an orthorhombic

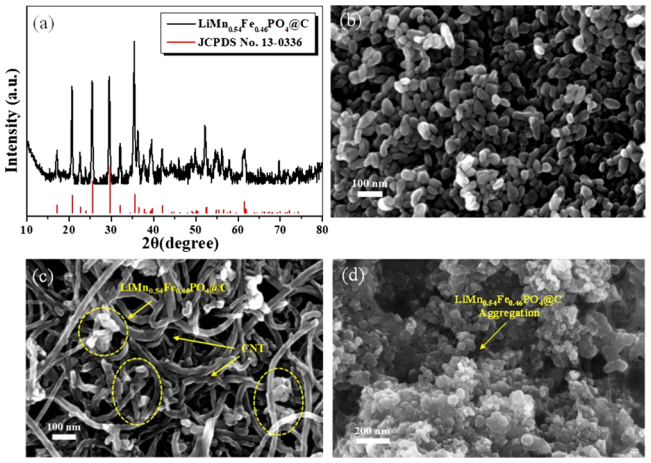

Figure 1. XRD pattern (a) and SEM images (b) of the LMFP@C powder. SEM images of the LMFP@C single particle electrode (c) and conventionally prepared electrode (d).

Pmnb space group is obtained without impurity phases in LMFP@C nanocrystals. The scanning electron microscopy (SEM) image (Figure 1b) exhibits the morphology of the LMFP@C, which are ellipsoid-shaped nanoparticles with a diameter of about 60 nm. The SEM image of the as-prepared ultrathin SP electrode is presented in Figure 1c. Figure S1 shows the transmission electron microscopy (TEM) image (a) and C (b), Fe (c), Mn (d) photoelectron spectroscopy patterns of the LMFP@C SP electrode; it can be clearly observed that the nanocrystals separated are uniformly distributed in the carbon nanotube network. As reported previously,[16] there are also many mesoporous (about 20−50 nm) and macroporous (about 100−300 nm) structures in the carbon nanotube network, which allows the nanocrystals to sufficiently make contact with the electrolyte so the concentration polarization from electrolyte can be minimized. In contrast, Figure 1d shows the morphology of the electrode prepared via the slurry-casting method, where severe aggregation of active material particles can be observed. The corresponding result also can be observed in Figure S2 through the TEM image (a) and C (b), Fe (c), Mn (d) photoelectron spectroscopy patterns of the LMFP@C conventionally prepared electrode.

In order to study the electrochemical kinetic of the electrode material, a cyclic voltammetry (CV) test for the SP LMFP@C electrode is carried out in a three-electrode system and the corresponding results are shown in Figure 2a. From the first cycle, two cathodic peaks can be found at 0.51 and 1.01 V, whereas two anodic peaks can be observed at 0.57 and 1.20 V, corresponding to the redox reactions Fe^{2+}/Fe^{3+} and Mn^{2+}/Mn^{3+}. As cycling continues, it can be seen that the peak current for the Mn^{2+}/Mn^{3+} redox couple diminishes rapidly, whereas the Fe^{2+}/Fe^{3+} peak starts to decay after the 10th cycle; then both peaks decline together. Figure 2b shows the charge−discharge curves of the SP electrode. It can be seen that the SP electrode suffers from severe capacity-fading, which is in good agreement with the CV result in Figure 2a. More importantly, the total capacity-fading also mainly comes from the capacity

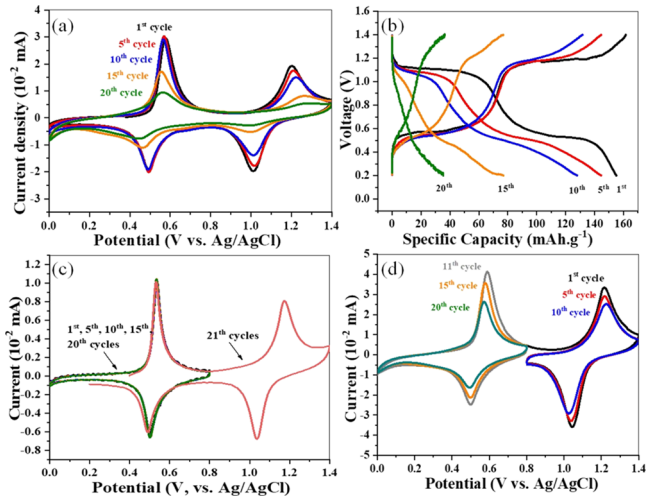

Figure 2. CV (a) and charge−discharge (b) curves of the LMFP@C SP electrode for the first 20 cycles. CV curves of the LMFP@C SP electrode in different potential ranges: (c) first scanned between 0 and 0.8 V for the first 20 cycles and then turned to 0−1.4 V for the 21st cycle; (d) first scanned between 0.8 and 1.4 V for the first 10 cycles and then turned to 0−0.8 V for the 11th to 20th cycles. The scan rate for all CV experiments is 1 mV s^{-1}.

loss for the Mn^{2+}/Mn^{3+} redox plateau. In addition, the ICP data (Table S1) reveal that about 12% Mn^{2+} was dissolved into the electrolyte after being cycled in a three-electrode system. The effect of Mn^{2+} dissolution has been widely reported for lithium manganese oxides;[17−19] however, it is seldom mentioned for LMFP-based cathode materials. Furthermore, to investigate Fe^{2+}/Fe^{3+} and Mn^{2+}/Mn^{3+} redox pairs separately, the testing voltage is first set between 0 and 0.8 V (vs Ag/AgCl), which corresponds to the redox region for Fe^{2+}/Fe^{3+}. As shown in Figure 2c, it is found that without the redox reaction of Mn, the intensity of the Fe peak remains almost unchanged during 20 cycles, indicating good reversibility of the Fe redox reactions in LMFP. The potential window is then set to between 0.8 and 1.4 V (vs Ag/AgCl) for another cycle, which corresponds to the Mn^{2+}/Mn^{3+} redox reaction. It is found that the peak currents of Mn redox reactions remain the same to those in Figure 2a. Next, the potential is first set between 0.8 and 1.4 V for 10 cycles and then set to the Fe^{2+}/Fe^{3+} redox region for another 10 cycles. As shown in Figure 2d, in contrast to Fe^{2+}/Fe^{3+}, current peaks for the Mn^{2+}/Mn^{3+} redox pair experience severe attenuation within 10 cycles. Then, the testing voltage is set back to the region for Fe^{2+}/Fe^{3+}; an instant fading can be observed. On the basis of the results above, it can be concluded that the fading phenomenon of the Mn peak subsequently induces the deterioration of the Fe redox peak. This could be because after a large amount of Mn dissolution, the crystal structure of LMFP becomes unstable, which further leads to the irreversible Fe redox behavior. For comparison, Figure S3 presents CV (a) and charge−discharge (b) curves of a conventionally prepared LMFP electrode. It can be observed that the conventionally prepared LMFP electrode shows great cyclic stability.

In order to further uncover the degradation mechanism of LMFP@C, XRD patterns of the SP LMFP@C electrode before and after full cycling are compared in Figure 3a. The diffraction peaks indicate that both samples are well assigned to the orthorhombic *Pmnb* space group. By comparing with the

DOI: 10.1021/acsami.8b18930
ACS Appl. Mater. Interfaces 2019, 11, 957−962

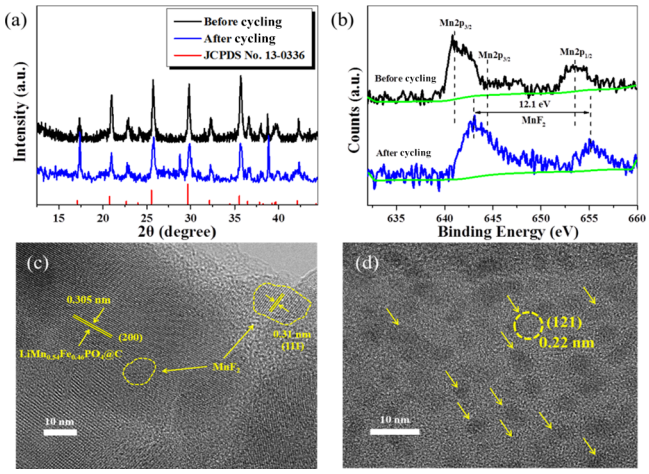

Figure 3. XRD (a) and Mn 2p XPS patterns (b) of the $LiMn_{0.54}Fe_{0.46}PO_4$@C SP electrode before and after cycling. HRTEM of $LiMn_{0.54}Fe_{0.46}PO_4$@C SP electrode after cycling (c,d).

pristine electrode, the SP electrode after full cycling shows an additional sharp peak at 28.7°, which can be assigned to the MnF_2 crystal phase. X-ray photoelectron spectrometry measurement is also carried out to determine the valence of the elements in the cycled electrode. As displayed in Figure 3b, the Mn 2p X-ray photoelectron spectroscopy (XPS) spectrum has a spin−orbit splitting component of Mn $2p_{1/2}$ at 653.5 eV and the shake-up satellites at about 641.1 and 644.4 eV are corresponding to Mn $2p_{3/2}$, which can be indexed to Mn^{2+}. After 20 cycles, the main peaks shift to 643.1 and 655.2 eV, and the multiplet splitting of the Mn 2p peak, which is the difference in binding energy between the Mn $2p_{1/2}$ and the Mn $2p_{3/2}$, is measured to be 12.1 eV. Since the probing depth of XPS technique is about several nanometers, this result can be attributed to the formation of a large amount of MnF_2 on the surface. Figure S4a presents the Fe $2p_{3/2}$ XPS spectrum; Fe peaks at 710.8 and 715.6 eV can be located at 687.8 eV, which can be indexed to the Fe^{2+} in the pristine electrode; the Fe peaks of the cycled sample shift to 713.9 eV, which can be ascribed to the FeF_3. The Li 1s spectra are shown in Figure S4b. The dominant binding energy of the cycled sample located at 58.7 eV can be assigned to the FeF_3. In addition, the intensity peaks at 55 and 56 eV can be ascribed to the Li 1s and LiF, respectively. The XPS spectrum of F 1s is presented in Figure S4c. For the pristine electrode, there is only one conspicuous peak that corresponds to the C−F chemical bond in the polyvinylidene fluoride (PVDF) binder. After cycling, an additional peak emerges at 685.7 eV, which was generally considered as the F−Li chemical bond. Figure 3c shows the TEM image of the LMFP@C composite after cycling. The measured lattice fringe spacing is 0.31 and 0.305 nm, which well match the (111) plane of MnF_2 (JCPDS no. 17-0864) and the (200) plane of LMFP, respectively. This finding further indicates the existence of the MnF_2 crystalline phase. In Figure 3d, many nanodomains with sizes of about 5 nm are found uniformly distributed in the single LMFP@C nanocrystal, which also can be assigned to the (121) plane of MnF_2 with a distinct lattice fringe spacing of 0.22 nm. Electrochemical impedance spectroscopy (EIS) is also carried out to characterize the electrochemical properties of LMFP@C. In Figure 4a, the Nyquist plots are measured at open circuit potential before cycling as well as after 5, 10, 15, and 20 cycles. It is noteworthy that the interfacial impedance of the SP LMFP@C electrode presented almost no change after 10 cycles, wherea the charge transfer impedance showed a continuous increasing trend, from 800 Ω after 5 cycles to 1250 Ω after 20 cycles. Therefore, it can be inferred that the accumulation of MnF_2 on the surface of LMFP impedes the Li ion transfer process, further resulting in continuous deterioration of its cycling capacity. Furthermore, the morphology of the SP electrode after cycling can be directly observed as shown in Figure 4b. It is apparent that the LMFP@C nanoparticles still maintain close contact with the carbon nanotube network but the surfaces of LMFP@C nanoparticles become rough and covered with some nanocrystallines.

On the basis of experimental results shown in Figure 2c,d, it can be inferred that the formation of MnF_2 is induced by the oxidized state of Mn. Moreover, the low Coulombic efficiencies during galvanostatic cycling also indicate capacity losses of Mn from a high oxidation state to a low oxidation state. Herein, a possible degradation mechanism of the LMFP@C composite is proposed in Figure 4c: generally, during the delithiation processes, Fe^{2+} and Mn^{2+} ions are oxidized to Fe^{3+} and Mn^{3+}. Mn^{3+} ions are disproportionate on the surface of the LMFP@C nanocrystals, forming Mn^{2+} and Mn^{4+}.[20−22] According to our previous work,[23] the soft X-ray absorption spectroscopy (sXAS) results show that using an aqueous electrolyte, Mn^{4+} can be measured on the cathode, whereas in the nonaqueous system, Mn^{4+} can be no longer detected. Therefore, it is reasonable to assume that owing to the strong oxidizing ability of Mn^{4+}, the organic solvent [e.g., ethylene carbonate (EC)] decomposes irreversibly via a ring-opening process on the surface of the LMFP particle, forming soluble Mn^{2+} salt [e.g., $Mn(OOCCH_3)_2$]. As it has been previously reported, an organic electrolyte with a trace amount of H_2O also contains a certain amount of hydrofluoric acid,[17] which can further react with dissolved Mn^{2+} salt to form insoluble MnF_2. In addition, the formation of MnF_2 is unfavorable for electronic and ionic transfer. As cycling continues, increasing amounts of MnF_2 nanocrystals and defects would occur on the surface of the LMFP nanocrystals. As these defects accumulate to a certain degree, new defects will emerge on the Fe sites, along with the formation of FeF_x. Owing to the intrinsic poor electronic conductivity and ionic diffusion coefficient of the pure LMFP, this type of degradation would result in the deterioration of the electronic and charge transfer process. In addition, to investigate the effect of fluoride in this process, an F-free electrolyte was prepared by replacing $LiPF_6$ into $LiClO_4$. From the results of CV (Figure 4d) and galvanostatic cycling (Figure S5), it can be seen that compared with the F^-containing electrolyte, the F-free electrolyte shows much slower capacity-fading for the SP electrode. More importantly, no nanodomains can be observed in the TEM images (as shown in Figure S6a,b) of LMFP nanoparticles after cycling. Both pieces of evidence further confirmed that fluorides in the electrolyte accelerate the surface reconstruction process for LMFP by forming insoluble MnF_2 on the surface of the LMFP nanoparticles.

For comparison, the normal thick electrode with dense LMFP nanoparticles aggregated was also studied. Measurements of XRD, XPS, and the dissolved percentage of Mn^{2+} of the normal electrode before and after cycling show no obvious change, shown in Figure S7 and Table S1. According to the above result, it can be learned that the SP electrode method could amplify the Mn^{2+} dissolution behavior, which is

DOI: 10.1021/acsami.8b18930
ACS Appl. Mater. Interfaces 2019, 11, 957−962

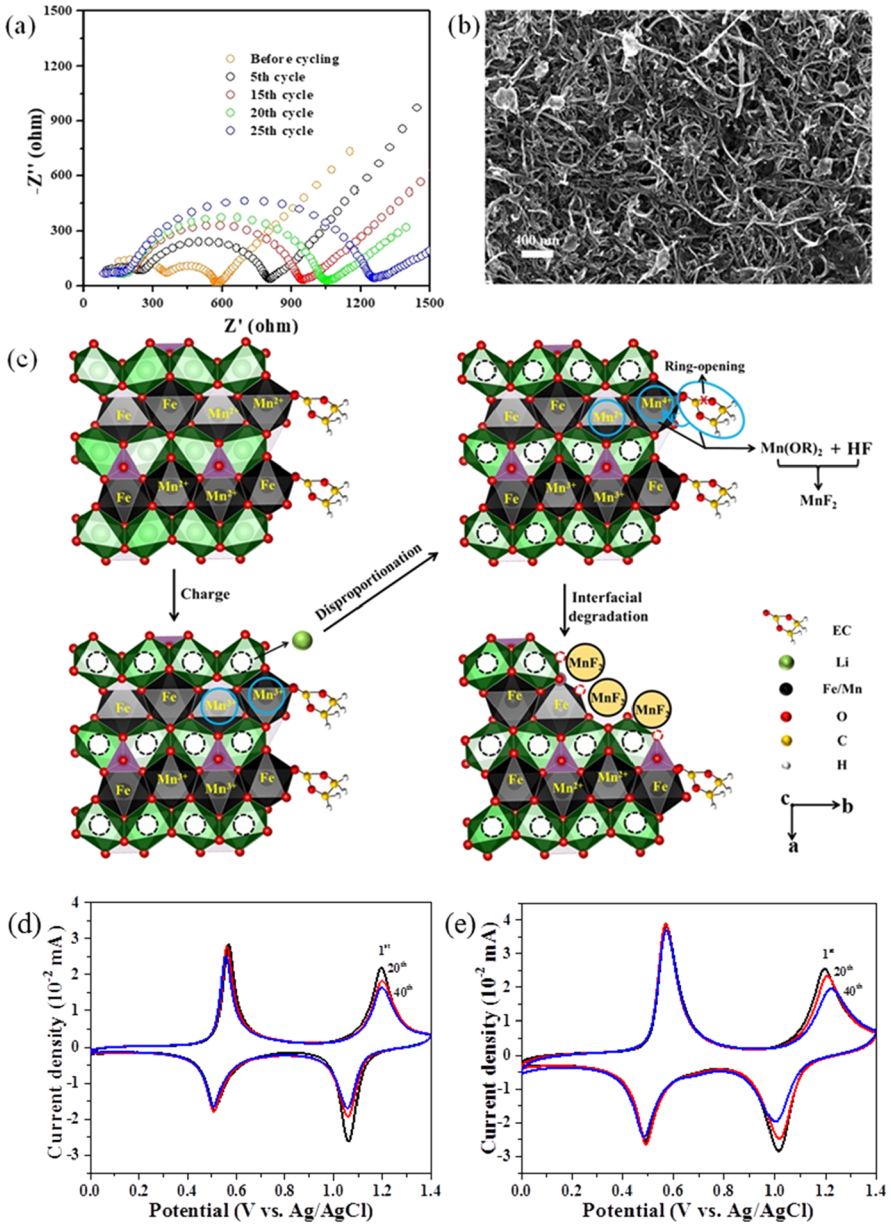

Figure 4. (a) EIS data of LMFP@C with different cycles, (b) SEM image of LMFP@C after 20 cycles, (c) proposed degradation mechanism of LMFP particles. (d) CV of LMFP@C for the first 40 cycles using 1 M $LiClO_4$ in EC/DMC v/v 1:1. (e) CV curves of ALD-modified LMFP@C for the first 40 cycles.

considered as the main cause of the capacity loss. This difference is due to the LMFP particles in SP electrode being fully in contact with the electrolytes; therefore, the Mn-ion dissolution is more prominent, whereas the aggregated LMFP particles have less exposed areas. Therefore, using the SP electrode is beneficial to investigate the intrinsic degradation mechanism of LMFP@C particles. In order to separate the electrolyte and the highly reactive sites on the cathode material, atomic layer deposition (ALD) technique was carried out to apply a thin Al_2O_3 protecting layer on the LMFP. The Al_2O_3 layer (about 5 nm) was uniformly coated on the surface of the LMFP@C nanocrystals and the corresponding TEM and photoelectron spectroscopy patterns are shown in Figure S8. Figure 4e shows the CV curves of the modified single-particle LMFP electrode at the scan rate of 1 mV s^{-1}. Moreover, compared with the pristine sample, the surface-coated sample shows superior cycling stability. The interfacial modification and protection of the current electrode material, especially for the electrode with a high cutoff voltage and accompanied by the severe transition metal dissolution behavior during electrochemical process, is an effective way to develop high-energy-density LIBs.[24]

CONCLUSIONS

To conclude, an ultrathin SP electrode is smartly designed and prepared to study the electrochemical behaviors of the LMFP material. It is found that the capacity-fading in the SP electrode is much faster than in the conventionally fabricated electrode. This difference may be attributed to the higher degree of surface degradation for LMFP, which not only reduces the capacity of the Mn redox pair, but also further leads to the capacity-fading for the Fe redox pair. In addition, the dissolution of Mn^{2+} also induces the formation of an MnF_2 passivation layer on the LMFP and inhibits the charge transfer

DOI: 10.1021/acsami.8b18930
ACS Appl. Mater. Interfaces 2019, 11, 957−962

at the surface of the LMFP particles. By applying a thin Al_2O_3 coating layer on the LMFP, the interfacial side reactions are effectively suppressed. This work demonstrates that the SP method is a useful technique to investigate interfacial reactions shrouded in oblivion.

EXPERIMENTAL METHODS

Material and SP Electrode Preparation. The LMFP nanoparticles were synthesized by the reflux method. A stoichiometric amount of $LiOH{\cdot}H_2O$, $FeSO_4{\cdot}7H_2O$, $MnSO_4$, and H_3PO_4 were dissolved into ethylene glycol and poured into a three-neck round-bottom flask. The above solution was continuously stirred for more than 6 h under 180 °C; then, the precipitates were washed by deionized water and ethyl alcohol several times and dried at 60 °C in vacuum. In order to obtain the LMFP@C composite, LMFP powders were dispersed into glucose solution by grinding for 1 h. A corundum crucible containing the dried mixture was heated to 650 °C for 6 h under Ar atmosphere.

To prepare the SP electrode, we first uniformly mixed the $LiMn_{0.54}Fe_{0.46}PO_4$@C nanoparticles and carbon nanotubes by grinding them for more than 30 min and then dispersing into a binder dilute solution with the ultrasonic time of more than 1 h. The mass ratio of the active material, carbon nanotube, and polyvinylidene fluoride binder was 3:2:2. Therefore, the key factors of the SP electrode were the deep-dispersed slurry and an ultrathin electrode. The conventionally fabricated electrode was prepared by uniformly mixing the $LiMn_{0.54}Fe_{0.46}PO_4$@C nanoparticles, acetylene black, and polyvinylidene fluoride with a mass ratio of 7:2:1.

Al_2O_3 Modification on Electrodes. An Al_2O_3 thin film was grown directly on electrodes in a home-built ALD reactor at 120 °C through 40 cycles. The reactor was continuous-flow and the base pressure of ~0.7 Torr was operated using argon gas. The precursors used for the Al_2O_3 ALD films were water (H_2O) and trimethylaluminum [(TMA), $Al(CH_3)_3$].

Characterization. The structure and phase characteristic of the samples were identified by the XRD using a Bruker D8 Advance diffractometer with a Cu Kα radiation source. The morphology of the LMFP@C particles and electrode were investigated by the SEM (ZEISS SUPRA 55). ICP optical emission spectrometry (ICP−AES, JY2000-2, HORIBA Jobin Yvon) measurement was used to detect the element content of the prepared samples. XPS (ESCALab220I-XL) was conducted to measure the chemical properties. The microstructure of the corresponding products was observed by the high-resolution TEM.

Electrochemical Measurement. A three-electrode system was chosen to investigate the electrochemical performance of the SP LMFP@C electrode. The LMFP@C electrode was used as working electrode, whereas the platinum electrode and Ag/AgCl were used as counter electrode and reference electrode, respectively. The electrolyte was an organic solution of 1 M $LiPF_6$ or $LiClO_4$ in EC and dimethyl carbonate (DMC) (v/v 1:1). CV and charging−discharging tests are carried out in the potential range of 0−1.4 V (vs Ag/AgCl). The EIS of the cycling three-electrode system was conducted on an electrochemistry workstation (CHI604E series, CH Instruments); the amplitude of the alternative current signal was 10 mV with the frequency range from 100 kHz to 0.01 Hz.

ASSOCIATED CONTENT

Supporting Information

The Supporting Information is available free of charge on the ACS Publications website at DOI: 10.1021/acsami.8b18930.

CV and charge−discharge curves of conventionally prepared LMFP electrode, ICP data, XPS data, and TEM images (PDF)

AUTHOR INFORMATION

Corresponding Authors

*E-mail: yangly.sz@pku.edu.cn (L.Y.).
*E-mail: panfeng@pkusz.edu.cn (F.P.).

ORCID

Luyi Yang: 0000-0002-5516-9829
Zheng Guo: 0000-0003-3802-1037
Feng Pan: 0000-0002-8216-1339

Author Contributions

†W.H. and J.H. contributed equally to this work.

Notes

The authors declare no competing financial interest.

ACKNOWLEDGMENTS

This work was financially supported by the National Key R&D Program of China (2016YFB0700600), the National Natural Science Foundation of China (no. 21603007 and 51672012), and the Shenzhen Science and Technology Research Grant (no. JCYJ20150729111733470, JCYJ20151015162256516).

REFERENCES

(1) Koltypin, M.; Aurbach, D.; Nazar, L.; Ellis, B. On the Stability of LiFePO[sub 4] Olivine Cathodes under Various Conditions (Electrolyte Solutions, Temperatures). *Electrochem. Solid-State Lett.* **2007**, *10*, A40−A44.

(2) Sun, C.; Rajasekhara, S.; Goodenough, J. B.; Zhou, F. Monodisperse Porous LiFePO4Microspheres for a High Power Li-Ion Battery Cathode. *J. Am. Chem. Soc.* **2011**, *133*, 2132−2135.

(3) Padhi, A. K.; Nanjundaswamy, K. S.; Goodenough, J. B. Phospho-olivines as Positive-Electrode Materials for Rechargeable Lithium Batteries. *J. Electrochem. Soc.* **1997**, *144*, 1188−1194.

(4) Sun, Y.-K.; Oh, S.-M.; Park, H.-K.; Scrosati, B. Micrometer-Sized, Nanoporous, High-Volumetric-Capacity LiMn0.85Fe0.15PO4 Cathode Material for Rechargeable Lithium-Ion Batteries. *Adv. Mater.* **2011**, *23*, 5050−5054.

(5) Aravindan, V.; Gnanaraj, J.; Lee, Y.-S.; Madhavi, S. LiMnPO4 - A next Generation Cathode Material for Lithium-Ion Batteries. *J. Mater. Chem. A* **2013**, *1*, 3518−3539.

(6) Mi, Y.; Gao, P.; Liu, W.; Zhang, W.; Zhou, H. Carbon nanotube-loaded mesoporous LiFe0.6Mn0.4PO4/C microspheres as high performance cathodes for lithium-ion batteries. *J. Power Sources* **2014**, *267*, 459−468.

(7) Shang, S. L.; Wang, Y.; Mei, Z. G.; Hui, X. D.; Liu, Z. K. Lattice Dynamics, Thermodynamics, and Bonding Strength of Lithium-Ion Battery Materials LiMPO $_4$ (M = Mn, Fe, Co, and Ni): A Comparative First-Principles Study. *J. Mater. Chem.* **2012**, *22*, 1142−1149.

(8) Delacourt, C.; Laffont, L.; Bouchet, R.; Wurm, C.; Leriche, J.-B.; Morcrette, M.; Tarascon, J.-M.; Masquelier, C. Toward Understanding of Electrical Limitations (Electronic, Ionic) in LiMPO[sub 4] (M=Fe, Mn) Electrode Materials. *J. Electrochem. Soc.* **2005**, *152*, A913−A921.

(9) Doan, T. N. L.; Bakenov, Z.; Taniguchi, I. Preparation of Carbon Coated LiMnPO4 Powders by a Combination of Spray Pyrolysis with Dry Ball-Milling Followed by Heat Treatment. *Adv. Powder Technol.* **2010**, *21*, 187−196.

(10) Yamada, A.; Chung, S.-C.; Liu, K.-Y. Crystal Chemistry of the Olivine-Type Li(Mn[sub y]Fe[sub 1−y])PO[sub 4] and (Mn[sub y]Fe[sub 1−y])PO[sub 4] as Possible 4 V Cathode Materials for Lithium Batteries. *J. Electrochem. Soc.* **2001**, *148*, A960.

(11) Xiang, W.; Wang, E.-H.; Chen, M.-Z.; Shen, H.-H.; Chou, S.-L.; Chen, H.; Guo, X.-D.; Zhong, B.-H.; Wang, X. Hierarchical Structured $LiMn_{0.5}Fe_{0.5}PO_4$ Spheres Synthesized by Template-Engaged Reaction as Cathodes for High Power Li-Ion Batteries. *Electrochim. Acta* **2015**, *178*, 353−360.

DOI: 10.1021/acsami.8b18930
ACS Appl. Mater. Interfaces 2019, 11, 957−962

(12) Meethong, N.; Huang, H.-Y. S.; Speakman, S. A.; Carter, W. C.; Chiang, Y.-M. Strain Accommodation during Phase Transformations in Olivine-Based Cathodes as a Materials Selection Criterion for High-Power Rechargeable Batteries. *Adv. Funct. Mater.* **2007**, *17*, 1115−1123.
(13) Choi, D.; Xiao, J.; Choi, Y. J.; Hardy, J. S.; Vijayakumar, M.; Bhuvaneswari, M. S.; Liu, J.; Xu, W.; Wang, W.; Yang, Z.; Graff, G. L.; Zhang, J.-G. Thermal stability and phase transformation of electrochemically charged/discharged LiMnPO4 cathode for Li-ion batteries. *Energy Environ. Sci.* **2011**, *4*, 4560−4566.
(14) Zheng, J.; Hou, Y.; Duan, Y.; Song, X.; Wei, Y.; Liu, T.; Hu, J.; Guo, H.; Zhuo, Z.; Liu, L.; Chang, Z.; Wang, X.; Zherebetskyy, D.; Fang, Y.; Lin, Y.; Xu, K.; Wang, L.-W.; Wu, Y.; Pan, F. Janus Solid-Liquid Interface Enabling Ultrahigh Charging and Discharging Rate for Advanced Lithium-Ion Batteries. *Nano Lett.* **2015**, *15*, 6102−6109.
(15) Duan, Y.; Zhang, B.; Zheng, J.; Hu, J.; Wen, J.; Miller, D. J.; Yan, P.; Liu, T.; Guo, H.; Li, W.; Song, X.; Zhuo, Z.; Liu, C.; Tang, H.; Tan, R.; Chen, Z.; Ren, Y.; Lin, Y.; Yang, W.; Wang, C.-M.; Wang, L.-W.; Lu, J.; Amine, K.; Pan, F. Excess Li-Ion Storage on Reconstructed Surfaces of Nanocrystals to Boost Battery Performance. *Nano Lett.* **2017**, *17*, 6018−6026.
(16) Hu, J.; Li, W.; Duan, Y.; Cui, S.; Song, X.; Liu, Y.; Zheng, J.; Lin, Y.; Pan, F. Single-Particle Performances and Properties of LiFePO4 Nanocrystals for Li-Ion Batteries. *Adv. Energy Mater.* **2017**, *7*, 1601894.
(17) Wang, E.; Ofer, D.; Bowden, W.; Iltchev, N.; Moses, R.; Brandt, K. Stability of Lithium Ion Spinel Cells. III. Improved Life of Charged Cells. *J. Electrochem. Soc.* **2000**, *147*, 4023−4028.
(18) Cho, I. H.; Kim, S.-S.; Shin, S. C.; Choi, N.-S. Effect of SEI on Capacity Losses of Spinel Lithium Manganese Oxide/Graphite Batteries Stored at 60°C. *Electrochem. Solid-State Lett.* **2010**, *13*, A168−A172.
(19) Shin, H.; Park, J.; Sastry, A. M.; Lu, W. Degradation of the Solid Electrolyte Interphase Induced by the Deposition of Manganese Ions. *J. Power Sources* **2015**, *284*, 416−427.
(20) Thackeray, M. M.; Johnson, P. J.; de Picciotto, L. A.; Bruce, P. G.; Goodenough, J. B. Electrochemical Extraction of Lithium from LiMn2O4. *Mater. Res. Bull.* **1984**, *19*, 179−187.
(21) Thackeray, M. M.; Shao-Horn, Y.; Kahaian, A. J.; Kepler, K. D.; Skinner, E.; Vaughey, J. T.; Hackney, S. a. Structural Fatigue in Spinel Electrodes in High Voltage (4 V) Li/Li[sub x]Mn[sub 2]O[sub 4] Cells. *Electrochem. Solid-State Lett.* **1998**, *1*, 7.
(22) Pigliapochi, R.; Seymour, I. D.; Merlet, C.; Pell, A. J.; Murphy, D. T.; Schmid, S.; Grey, C. P. Structural Characterization of the Li-Ion Battery Cathode Materials $LiTi_xMn_{2-x}O_4$ ($0.2 \leq X \leq 1.5$): A Combined Experimental ^{7}Li NMR and First-Principles Study. *Chem. Mater.* **2017**, *30*, 817−829.
(23) Zhuo, Z.; Hu, J.; Duan, Y.; Yang, W.; Pan, F. Transition Metal Redox and Mn Disproportional Reaction in LiMn0.5Fe0.5PO4electrodes Cycled with Aqueous Electrolyte. *Appl. Phys. Lett.* **2016**, *109*, 023901.
(24) Su, Y.; Cui, S.; Zhuo, Z.; Yang, W.; Wang, X.; Pan, F. Enhancing the High-Voltage Cycling Performance of LiNi0.5Mn0.3-Co0.2O2 by Retarding Its Interfacial Reaction with an Electrolyte by Atomic-Layer-Deposited Al2O3. *ACS Appl. Mater. Interfaces* **2015**, *7*, 25105−25112.

DOI: 10.1021/acsami.8b18930
ACS Appl. Mater. Interfaces 2019, 11, 957−962